



OPEN

Galerkin finite element analysis for magnetized radiative-reactive Walters-B nanofluid with motile microorganisms on a Riga plate

Faisal Shahzad¹, Wasim Jamshed^{1✉}, Usman², Rabha W. Ibrahim³, Farheen Aslam⁴, El Sayed M. Tag El Din⁵, Hamiden Abd El-Wahed Khalifa^{6,7} & Fayza Abdel Aziz ElSeabee^{8,9}

In order to understand the characteristics of bio-convection and moving microorganisms in flows of magnetized Walters-B nano-liquid, we developed a model employing Riga plate with stretchy sheet. The Buongiorno phenomenon is likewise employed to describe nano-liquid motion in the Walters-B fluid. Expanding correspondence transformations, the partial differential equation (PDE) control system has been transformed into an ordinary differential equation (ODE) control system. The COMSOL program is used to generate mathematical answers for non-linear equations by employing the Galerkin finite element strategy (G-FEM). Utilizing logical and graphical metrics, temperature, velocity, and microbe analysis are all studied. Various estimates of well-known physical features are taken into account while calculating nanoparticle concentrations. It is demonstrated that this model's computations directly relate the temperature field to the current Biot number and parameter of the Walters-B fluid. The temperature field is increased to increase the approximations of the current Biot number and parameter of the Walters-B fluid.

List of symbols

α	Viscoelastic parameter
E	Activation energy (K J mol^{-1})
H	Modified Hartman number
λ_c	The relaxation time of mass (s)
K_1, K_2	Homogeneous and heterogeneous reactions
T	Liquid temperature (K)
C	Liquid concentration (kg m^{-3})
T_∞	Ambient temperature (K)
C_∞	Ambient concentration (kg m^{-3})
D_B	Coefficient of diffusion ($\text{m}^2 \text{s}^{-1}$)
q	Heat flux ($\text{J m}^{-2} \text{s}^{-1}$)
J	Mass flux ($\text{kg m}^{-2} \text{s}^{-1}$)
ρ	Density (kg m^{-3})
p	Pressure ($\text{Kg m}^{-1} \text{s}^{-2}$)
C_p	Specific heat capacity ($\text{J kg}^{-1} \text{K}^{-1}$)
k	Thermal conductivity of the liquid ($\text{W m}^{-1} \text{K}^{-1}$)

¹Department of Mathematics, Capital University of Science and Technology (CUST), Islamabad 44000, Pakistan. ²Department of Computer Science, National University of Sciences and Technology, Balochistan Campus (NBC), Quetta 87300, Pakistan. ³Near East University, Mathematics Research Center, Department of Mathematics, Near East Boulevard, Nicosia/Mersin 10 PC: 99138, Turkey. ⁴Department of Biotechnology, Lahore College for Women University, Lahore 54000, Pakistan. ⁵Electrical Engineering, Faculty of Engineering and Technology, Future University in Egypt, New Cairo 11835, Egypt. ⁶Department of Operations Research, Faculty of Graduate Studies for Statistical Research, Cairo University, Giza 12613, Egypt. ⁷Department of Mathematics, College of Science and Arts, Al-Badaya, Qassim University, Buraydah 51951, Saudi Arabia. ⁸Mathematics Department, Faculty of Science, Helwan University, Cairo, Egypt. ⁹Department of Mathematics, College of Science and Arts, Alasyah, Qassim University, Buraydah, Saudi Arabia. ✉email: wasiktk@hotmail.com

Nanofluids (NFs) are being considered as a viable liquid replacement that might raise the ability and effectiveness of current systems in manufacturing, commercial, and residential settings. Developed thermal system efficiency has many advantages, including lessening the negative effects on the environment, using less energy, and spending less money. The cost and environmental effect of NFs were assessed using sustainability methods to evaluate whether they were appropriate for use in thermal systems. Studies of heat are among its most important uses. Thermal systems' energy utilization is essential to the global ecology. Increased heat surface area is one of the most investigated methods for improving thermal exchangers' thermal presentation; yet, this modification results in significant accumulation and drives up manufacturing costs. Recent developments in solar collectors and the usage of NF were discussed by Gupta et al.¹. They discovered that the most effective strategy to boost the performance of a solar energy system is to employ a premium heat transfer fluid with remarkable thermophysical characteristics, such as high thermal conductivity, and NF is the best option for doing so. By lowering the heat of the liquid leaving the condenser, according to Salilih et al.², the use of NF boosted the effectiveness of the solar scheme. Olabi et al.³ conducted research on waste heat recovery, or the process of recovering energy losses as heat, work, or power. They asserted that the high-performance heat transfer (HT) fluids known as NFs had only recently been created. It is recommended that heat transfer development or inhibition as well as the usage of NFs be applied to various types of temperature pipes in accordance with the hypothesis advanced by Wang et al.⁴. The application of machine learning is explored in NFs (thermal conductivity and dynamic viscosity) and NF-charged heat pipes. Souza et al.⁵ looked at the most current advancements in NF thermal properties and applications in a range of engineering sectors, from NF-medicine to renewable energy. The latter has seen some significant improvements in mobility and propulsion, with ramifications for military and defense technologies. In a sono heat exchanger, Nugroho et al.⁶ looked at how ultrasonic waves affected the HT and NFs stability of MWCNTs. In their study Reddy et al.⁷ examined the properties of energy and sticky dissipation on the MHD HT of NFs movement over a nonlinear expanding surface with chemical reaction.

The constitutive associations of Maxwell are insufficient to characterize a large number of viscoelastic fluids. Elastico-viscous fluids come in two different varieties: Rivlin-Ericksen and Walters' B fluids model (WBFM). According to Walters⁸, a mixture of polymethyl methacrylate and pyridine with a density of 0.98 g per litre and 30.5 g of polymer per litre performs nearly identically to WBFM at 25 °C. WBFM is utilized to produce a number of necessary polymers and priceless products. The heat particle statement analysis for nonlinear thermally industrialized flow of WBFM with resistance powers was described by Chu et al.⁹. Waqas et al.¹⁰ explored the reactions in the WBFM with nonlinear heat energy and motivation dynamism bio-convection immobility point slip flow. The heat of ferromagnetic WBFM was highlighted by Siddique et al.¹¹ by changing current categorization. The stability physiologies of WBFM in a cylindrical figure with thermal transfer were studied by Awasthi et al.¹². Ahmad et al.¹³ noted that relative growth for the energy and attentiveness contours was suggested by the non-axisymmetric flow of unstable WBFM over a vertical cylindrical disk. An accurate characterization of the electro-osmotic flow of the WBFM with a non-singular kernel was reported by Sunthrayuth et al.¹⁴. The unproductivity point of WBFM over power-law filing exterior with slip situations was inspected by Ahmad et al.¹⁵. Utilizing the guidance of strange recreation analysis, Idowu and Falodun¹⁶ observed the Soret-Dufour properties on MHD heat and mass transmission of WBFM over a semi-infinite perpendicular disc. For more details see Refs.^{17–26}.

An electromagnetic shallow known as a Riga plate (RP) is used to alternatively build electrodes. This setup results in electromagnetic hydrodynamic behavior in the fluid flow. In this investigation, the effects of thermal radiation, melting heat, and viscous dissipation on the RP are examined. Akolade and Tijani²⁷ considered RP in a comparative study of three-dimensional flow of Casson–Williamson NFs. Hakeemet al.²⁸ presented RP in 3D- viscous dissipative movement of NFs. Rawat et al.²⁹ introduced a numerical study of thermal radiation and suction effects on copper and silver water NFs over RP. Rasool and Zhang³⁰ considered the RP to characterize the chemical reaction and convective boundary conditions in Powell-Eyring NFs movement. Asogwa et al.³¹ suggested a proportional examination of aquatic constructed Al₂O₃ NFs through water created CuO NFs via enhanced radiate RP.

In contrast to heterogeneous reactions (HHRs), which have reactants in two or more phases, homogeneous reactions are chemical processes in which the reactants and products are in the same phase. Heterogeneous reactions are those that happen on the surface of a catalyst made of a dissimilar level. Anuar et al.³² considered NFs stagnation point movement via MHD stretching/shrinking sheet in presence of HHRs. Mishra et al.³³ analyzed HHRs in a NFs past a nonlinear widening shallow. Almutairi et al.³⁴ utilized MHD movement of NFs with HHRs in a porous medium further down the effect of second-order velocity slide. Li et al.³⁵ modified the motion of NFs with HHRs. Raeeset al.³⁶ suggested a HHR model for assorted convection in gravity-driven film movement of NFs.

A procedure called bioconvection addresses the wave of mobile microorganisms, which might be useful in preventing the likely relaxing of NFs entities. Waqas et al.^{37–43} considered this process in different studies via various types of NFs, such as Carreau–Yasuda, Casson, Buongiorno and Oldroyd-B NFs. Analysis and numerical studies using different mathematical modeling are given by Beg et al.⁴⁴, Sajid et al.⁴⁵, Waqas et al.⁴⁶, Khan et al.⁴⁷ and Imran et al.⁴⁸. Muhammad et al.⁴⁹ presented a study on especially stratified bioconvective transference of Jeffrey NFs with gyrostatic motile microorganisms. Rao et al.⁵⁰ indicated the bioconvection in a convective NFs movement containing gyrotactic microorganisms done by an isothermal perpendicular funnel entrenched in an absorbent shallow with chemical reactive type. Recent additions consider nanofluids with heat and mass transfer in various physical situations^{51–54}.

The Finite element method (FEM) is a general arithmetical approach for answering PDEs in two or three spatial variables. All mathematical modeling systems, especially those involving mass and heat movement, heavily employ this technique. It first appeared in Ahmad's study⁵⁵, where the goal was to use FEM to simulate the NFs movement and heat arenas inside a motivated geometry that was home to a heat-generating device. Using the generalized FEM, Hiba et al.⁵⁶ optimized hybrid NFs. The melting effect on CCHF and heat energy types for

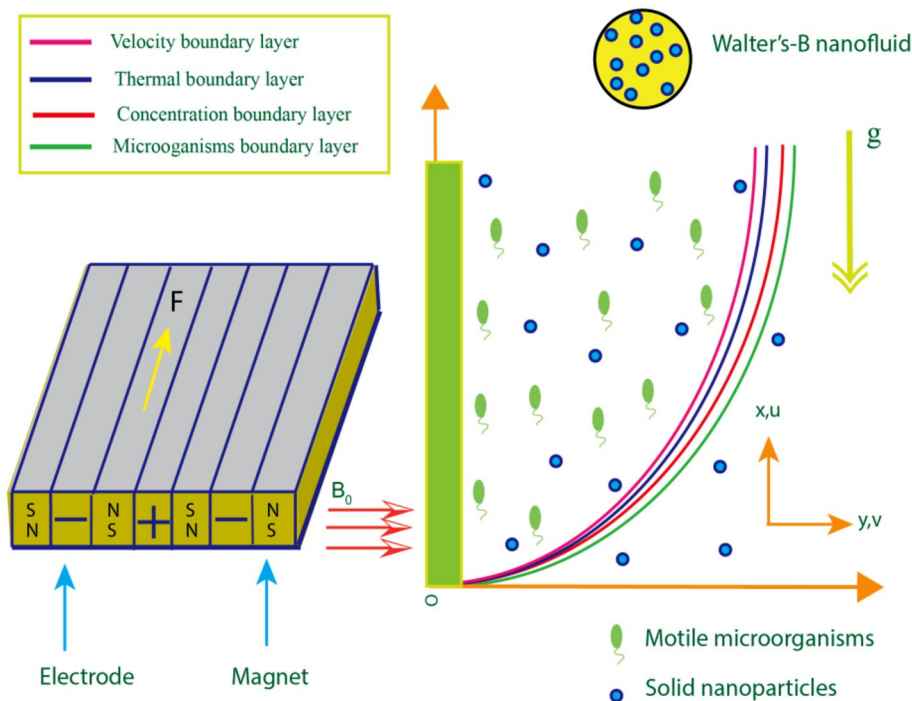


Figure 1. Flow chart for a current problem.

allied MHD NFs movement was measured by Ali et al.⁵⁷ using the FEM methodology. Using FEM, Abderrahmane et al.⁵⁸ achieved the best result for non-Newtonian NFs. With the aid of FEM, Rana and Gupta⁵⁹ created a solution for the quadratic convective and active movement of hybrid NFs over a rotating pinecone. On a widening shallow of Chamfer flippers, Pasha and Domiri-Ganji⁶⁰ used FEM to study a hybrid NF. In an animated inclusion with switch cylindrical cavity, Redouane et al.⁶¹ investigated the thermal movement flood of hybrid NFs under the assumption of generalized FEM. Using FEM, Alrowaili et al.⁶² demonstrated a magnetic radioactive convection of NFs. A dynamic system of NFs was modeled by Zaaroura et al.⁶³ using a FEM-optimized homogenization technique. Using FEM simulation, Ahmed and Alhazmi⁶⁴ impacted the revolution and various heat conditions of rolls with glass spheres in the presence of radioactivity.

The prior literature demonstrates that the properties of bio-convection and moving microorganisms in flows of magnetized Walters-B nano-liquid with convective border constraints were not before studied. To close this gap in the interpretation, the Walters-B nanofluid and the heat diffusion theory in the presence of Brownian and thermophoretic diffusion were both included. A stretchable sheet with Riga plate was employed in the current experiment to simulate the physical state. This work is very beneficial in many different technological and industrial domains. The higher-order nonlinear ODEs that were produced were solved with COMSOL software to generate G-FEM solutions for nonlinear equations. Graphical representations were used to show the effects of various flow parameters on the velocity, temperature, and concentration of Walters-B nanofluid. Additionally, the Walters-B nanofluid's Nusselt, Sherwood, and consistency quantities were determined and examined.

Governing equations and material

Use a 2D steady flow of magnetized Walters-B nano-liquid across a stretchy surface to examine the characteristics of bio-convection and migrating microorganisms along the fluid flow in x -path. With a stretching speed of $u = U$ $w = cx$, the xy -coordinate system is utilized, with the x -axis parallel to the flowing direction and the y -axis parallel to the flowing path, as illustrated in Fig. 1. The magnetic field has been subjected to B_0 . The Walters-B nanofluid is expected to be in a diluted suspension due to a uniform distribution of gyrotactic microorganisms. When suspended nanoparticle concentrations are less than 1%, gyrotactic bacteria' swimming velocity and orientation are unaffected by nanoparticles. It is also hypothesized that when the suspended nanoparticles concentration is low, the bio convection effect is exacerbated. Both the wall's temperature (T_w) and concentration (C_w) are kept constant. There are two cooled extended surface scenarios: $T_w < T_\infty$ and $C_w < C_\infty$. The impacts of activation energy and bilateral reaction are anticipated to be significant due to the study's anticipated high species concentration. Where the width of the magnets is placed in the space between the electrodes, represents the magnetic property of the permanent magnets' plate surface, and represents the amount of current flowing through the electrodes. Where r_0 denotes the width of the magnets positioned in the interval separating the electrodes, M_0 denotes plate surface magnetic property of the permanent magnets, j_0 denotes current density applied to the electrodes.

In view of the proposed assumptions, the governing equations and corresponding boundary conditions for Walters-B nanofluid flowing following^{65,66}

$$\frac{\partial u}{\partial x} + \frac{\partial v}{\partial y} = 0, \tag{1}$$

$$\left. \begin{aligned} u \frac{\partial u}{\partial x} + v \frac{\partial u}{\partial y} &= v \frac{\partial^2 u}{\partial y^2} - \frac{k_0}{\rho} \left(u \frac{\partial^3 u}{\partial x \partial y^2} + v \frac{\partial^3 u}{\partial y^3} + \frac{\partial u}{\partial x} \frac{\partial^2 u}{\partial y^2} - \frac{\partial u}{\partial y} \frac{\partial^2 u}{\partial x \partial y} \right) - \frac{\sigma B_0^2}{\rho} (u - U_e) \\ + U_e \frac{dU_e}{dx} + \frac{1}{\rho_f} &\left[(\rho_f \beta^{**}) g^* (T - T_\infty) - \frac{M_p (\rho_p - \rho_f) g^*}{\rho_p} (C - C_\infty) - \gamma (\rho_m - \rho_f) g^* (N - N_\infty) \right] \\ &+ \frac{\pi j_0 M}{8 \rho} e^{-\frac{\pi}{r_0} y}, \end{aligned} \right\} \tag{2}$$

$$\left. \begin{aligned} u \frac{\partial T}{\partial x} + v \frac{\partial T}{\partial y} &= \alpha \frac{\partial^2 T}{\partial y^2} + \frac{\partial}{\partial y} \left(\frac{16 \alpha \sigma^* T_\infty^3}{3 k^*} \frac{\partial T}{\partial y} \right) + \frac{Q_0}{\rho C_p} (T - T_\infty) + \lambda_t^* \frac{Q_0}{\rho C_p} \left(v \frac{\partial T}{\partial y} + u \frac{\partial T}{\partial x} \right) \\ + \lambda_t^* \tau D_B &\left(u \frac{\partial^2 C}{\partial x \partial y} \frac{\partial T}{\partial y} + u \frac{\partial C}{\partial y} \frac{\partial^2 T}{\partial x \partial y} + v \frac{\partial^2 C}{\partial y^2} \frac{\partial T}{\partial y} + v \frac{\partial C}{\partial y} \frac{\partial^2 T}{\partial y^2} \right) \\ + \lambda_t^* \tau \frac{D_T}{T_\infty} &\left(\frac{\partial T}{\partial y} \right)^2 + 2 \lambda_t^* \tau \frac{D_T}{T_\infty} \left[u \frac{\partial T}{\partial y} \frac{\partial^2 T}{\partial y^2} + v \frac{\partial^2 T}{\partial y^2} \frac{\partial T}{\partial y} \right], \end{aligned} \right\} \tag{3}$$

$$\left. \begin{aligned} u \frac{\partial C}{\partial x} + v \frac{\partial C}{\partial y} &= D_B \frac{\partial^2 C}{\partial y^2} + \lambda_c^* \frac{D_T}{T_\infty} \left(\frac{\partial^2 T}{\partial y^2} + \frac{\partial v}{\partial y} \frac{\partial^2 T}{\partial y^2} + \frac{\partial u}{\partial y} \frac{\partial^3 T}{\partial x \partial y} \right) \\ - K r^2 (C - C_\infty) &\left(\frac{T}{T_\infty} \right)^n \exp\left(\frac{-E_a}{kT}\right) - \lambda_c^* k_c \left(v \frac{\partial C}{\partial y} + u \frac{\partial C}{\partial x} \right) - \lambda_c^* \left[u^2 \frac{\partial^2 C}{\partial x^2} \right. \\ + v^2 \frac{\partial^2 C}{\partial y^2} &+ 2uv \frac{\partial^2 C}{\partial x \partial y} + \frac{\partial C}{\partial x} \left(u \frac{\partial u}{\partial x} + v \frac{\partial u}{\partial y} \right) + \frac{\partial C}{\partial y} \left(u \frac{\partial v}{\partial x} + v \frac{\partial v}{\partial y} \right) \left. \right], \end{aligned} \right\} \tag{4}$$

$$u \frac{\partial N}{\partial x} + v \frac{\partial N}{\partial y} + \frac{b W_c}{(C_w - C_\infty)} \left[\frac{\partial}{\partial y} \left(N \frac{\partial C}{\partial y} \right) \right] = D_m \frac{\partial^2 N}{\partial y^2}. \tag{5}$$

$$u \frac{\partial a}{\partial x} + v \frac{\partial a}{\partial y} = D_A \frac{\partial^2 a}{\partial y^2} - K_c a b^2, \tag{6}$$

$$u \frac{\partial b}{\partial x} + v \frac{\partial b}{\partial y} = D_B \frac{\partial^2 b}{\partial y^2} + K_c a b^2, \tag{7}$$

having boundary conditions⁶⁷

$$\left. \begin{aligned} u = U_w = cx, v = 0, -k \frac{\partial T}{\partial y} &= h_f (T_w - T), D_A \frac{\partial a}{\partial y} = K_s a, \\ D_B \frac{\partial b}{\partial y} = -K_s a, -D_B \frac{\partial C}{\partial y} &= h_g (C_w - C), -D_m \frac{\partial N}{\partial y} = h_n (N_w - N) \text{ at } y = 0 \\ u \rightarrow U_e = bx, \frac{\partial u}{\partial y} \rightarrow 0, T &\rightarrow T_w, C \rightarrow C_w, N \rightarrow N_w, a \rightarrow a_0, b \rightarrow 0 \text{ as } y \rightarrow \infty. \end{aligned} \right\} \tag{8}$$

The above governing equations are solved by following suitable transformations:

$$\left. \begin{aligned} \Upsilon &= y \sqrt{\frac{c}{v}}, u = cx f', v = -\sqrt{cv} f, \theta = \frac{T - T_\infty}{T_w - T_\infty}, \\ \phi &= \frac{C - C_\infty}{C_w - C_\infty}, \chi = \frac{N - N_\infty}{N_w - N_\infty}, a = a_0 h(\eta), b = b_0 q(\eta). \end{aligned} \right\} \tag{9}$$

Here f, θ, ϕ , and χ are functions of Υ . Following equations are obtained.

$$f''' - M f' - (f')^2 + f f'' + \alpha (2 f' f''' - f f^{iv} - (f'')^2) - \lambda (\theta - N r \phi - N c \chi) + M K + K^2 + \text{Hexp}(-\Lambda \Upsilon) = 0, \tag{10}$$

$$\left. \begin{aligned} (1 + \frac{4}{3} R d) \theta'' + \text{Pr} (\delta_1 \theta + f \theta') + \text{Pr} [-N b (f \theta' \phi'') \\ - f \theta'' \phi'] + 2 N t f' \theta' \theta'' - (f^2 \theta'' - f f' \theta') = 0 \end{aligned} \right\} \tag{11}$$

$$\left. \begin{aligned} \phi'' + \text{LePr} [-f \phi' - \sigma^* (1 + \mu \theta)^n \exp(\frac{-E}{1 + \mu \theta}) \phi - \lambda_c K_c f \phi'] \\ + \text{LePr} \lambda_c [-f^2 \phi'' - f f' \phi - \text{LePr} \frac{N t}{N b} (\theta'' + f' \theta'')] = 0, \end{aligned} \right\} \tag{12}$$

$$\chi'' + L b f \chi' - P e [(\chi + \omega) \phi'' + \chi' \phi'] = 0. \tag{13}$$

$$\frac{1}{Sc} h'' + \frac{2}{3} f l' - K h q^2 = 0, \tag{14}$$

$$\frac{\delta^*}{Sc} q'' + \frac{2}{3} f q' + K h q^2 = 0, \tag{15}$$

With boundary conditions

$$\left. \begin{aligned} f = 0, f' = 1, \theta' = -\gamma_1(1 - \theta(\Upsilon)), \phi' = -\gamma_2(1 - \phi(\Upsilon)), \\ h'(\eta) = K_1 h, \delta q'(\eta) = -K_1 h, \chi' = -\gamma_3(1 - \chi(\Upsilon)) \text{ at } \Upsilon = 0, \\ f' \rightarrow K, f'' \rightarrow 0, \theta \rightarrow 0, \phi \rightarrow 0, \chi \rightarrow 0, h(\eta) \rightarrow h, q(\eta) \rightarrow 0 \text{ as } \Upsilon \rightarrow \infty. \end{aligned} \right\} \quad (16)$$

In most cases, the diffusion coefficients $D_A=D_B$ gives $\delta = 1$. The following relation can be achieved after the implementation of this assumption.

$$h(\eta) + q(\eta) = 1, \quad (17)$$

utilizing (17) in (14) and (15) gives

$$\frac{1}{Sc} h'' + \frac{2}{3} fh' - K_1 h(1 - h)^2 = 0, \quad (18)$$

whereas boundary conditions are bestowed by

$$h'(0) = K_2 h(0), h(\infty) = 1. \quad (19)$$

Different dimensionless parameters arising in (9)–(13) are given underneath:

$$\left. \begin{aligned} \alpha &= \frac{cK_0}{\mu}, K = \frac{b}{c}, M = \sqrt{\frac{\sigma B_0^2}{\rho_f}}, H = \frac{\pi j_0 M_0}{8\rho U_w^2}, \Lambda = \sqrt{\frac{\pi^2 v}{a^2 c}} \\ \lambda &= \frac{(1-C_\infty)\beta^{**}g^*(T_w-T_\infty)}{c^2 x}, Nr = \frac{(\rho_p-\rho_f)g^*(C_w-C_\infty)}{(1-C_\infty)\beta^{**}\rho_f(T_w-T_\infty)}, \\ \delta_1 &= \frac{Q_0}{c\rho C_p}, Pr = \frac{\nu}{\alpha}, Nc = \frac{(\rho_m-\rho_f)\gamma(N_w-N_\infty)}{(1-C_\infty)\beta^{**}\rho_f(T_w-T_\infty)}, \\ Nb &= \frac{\tau D_B(C_w-C_\infty)}{\nu}, Rd = \frac{4\sigma^* T_\infty^3}{k^*}, Nt = \frac{\tau D_T(T_w-T_\infty)}{\nu T_\infty}, \\ \lambda_C &= c\lambda_c^*, Le = \frac{\alpha}{D_B}, E = \frac{-E_a}{\kappa T_\infty}, \mu = \frac{(T_w-T_\infty)}{T_\infty}, \sigma^* = \frac{Kr^2}{c}, Sc = \frac{\nu}{D_B}, \\ \frac{Nt}{Nb} &= \frac{D_T(T_w-T_\infty)}{D_B T_\infty(C_w-C_\infty)}, Lb = \frac{\nu}{D_m}, Pe = \frac{bW_c}{D_m}, K_1 = \frac{K_c a_0}{x^{\frac{2}{3}}}, K_2 = \frac{K_s a_0^2}{l}. \end{aligned} \right\} \quad (20)$$

where α is a viscoelastic parameter while K is a velocity ratio parameter. $M, H, \Lambda, Nr,$ and Nc are signifying magnetic field parameter, modified Hartman number, dimensionless parameter, Buoyancy ratio number, and rayleigh number of bioconvection, respectively. Pr is the Prandtl number, while Nb is utilized as a parameter for Brownian motion. δ_1 is used for a different number of microorganisms, whereas Rd is a parameter for thermal radiation. Le and E are showing as Lewis number and activation energy. μ is the temperature difference parameter while σ^* is a chemical reaction factor. Lb is the Lewis parameter of bio-convection, and Pe is used as the Peclet parameter. Also, $\gamma_1, \gamma_2, \gamma_3, Nt$ and λ are signifying Biot number of heat, Biot number of solution, Biot number of microorganisms, Thermophoresis parameter, and parameter of mixed convection, K_1 and K_2 denotes the parameters of homogeneous and heterogeneous reactions, respectively.

Galerkin-finite element method (G-FEM)

The corresponding boundary constraints of the present system were computational simulated using FEM. FEM is based on partitioning the desired region into components (finite). FEM⁶⁸ is covered in this section. Figure 2 depicts the flow chart of the finite element method. This method has been employed in numerous computational fluid dynamics (CFD) issues; the benefits of employing this strategy are discussed further below.

Weak form is derived from strong form (stated ODEs), and residuals are computed. To achieve a weak form, shape functions are taken linearly, and FEM is used. The assembly method builds stiffness components, creating a global stiffness matrix. An algebraic framework (nonlinear equations) is produced using the Picard linearizing technique. Algebraic equations are simulated utilizing appropriate halting criterion through 10^{-5} (supercomputing tolerances).

$$\left| \frac{\Upsilon_{i+1} - \Upsilon_i}{\Upsilon^i} \right| < 10^{-5}.$$

Further, The Galerkin finite element technique’s flow chart is depicted in Fig. 2.

Validity of code

The validity of the computational technique was determined by comparing the heat transmission rate from the existing method to the verified consequences of earlier investigations⁶⁹⁻⁷¹. A comparison of current research outcomes with the previous study results is shown in Table 1. The current study is comparable and presented highly accurate results.

The important physical parameters in this problem are the local heat and mass fluxes, as well as the local motile microorganisms flux, which are specified as:

$$Nu_x = \frac{xq_w}{k(T_w - T_\infty)}, Sh_x = \frac{xq_m}{D_B(\phi_w - \phi_\infty)}, Nn_x = \frac{xq_n}{D_m(N_w - N_\infty)} \quad (21)$$

in which

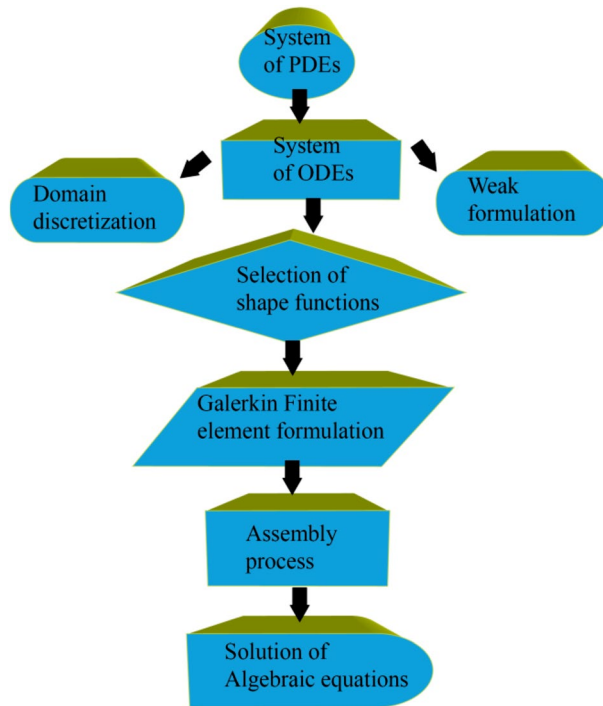


Figure 2. Flow chart of G-FEM.

P_r	Das et al. ⁶⁹	Qureshi ⁷⁰	Hussian ⁷¹	This study
0.72	0.80876122	0.8087618	0.8087618	0.8087612
1.0	1.00000000	1.0000000	1.0000000	1.0000000
3.0	1.92357431	1.9235742	1.9235742	1.9235734
7.0	3.07314679	3.0731465	3.0731465	3.0731465
10	3.72055436	3.7205542	3.7205542	3.7205511

Table 1. Comparing $-\theta'(0)$ with alteration in Prandtl number, and taking $\delta_1 = Rd = Nt = \gamma_1 = \gamma_2 = \gamma_3 = 0$ and $Nb = 0$.

$$q_w = -k \left(\frac{\partial T}{\partial y} \right)_{y=0}, q_m = -D_B \left(\frac{\partial \phi}{\partial y} \right)_{y=0}, q_n = -D_m \left(\frac{\partial N}{\partial y} \right)_{y=0}. \tag{22}$$

Using the similarity transform presented above, Eq. (23) can be described as:

$$Nu_x Re_x^{-1/2} = -\theta'(0), Sh_x Re_x^{-1/2} = -\phi'(0), Nn_x Re_x^{-1/2} = -\chi'(0) \tag{23}$$

Results and discussion

This portion of the analysis demonstrates the effects of the pertinent parameters on the dimensionless boundary layer distributions.

Figures 3, 4 are depicted to analyze the effects of the modified Heart number H on the velocity $f'(\Upsilon)$ and temperature $\theta(\Upsilon)$. It is worth illustrating that the profile $f'(\Upsilon)$ is enhancing for enhancing values of the parameter H , whereas the profile $\theta(\Upsilon)$ decays. An acceleration is noticed in the velocity as the strength of the parameter H is escalated. This makes good sense given the physics of the problem, $H > 0$ aids the flow phenomena during flow dispersion. This trend demonstrates that upon escalating the strength of the parameter H , the outward electric field becomes stronger. The velocity profile grew as a result. In these conditions, the magnetic field's strength and electromagnetic field increase equivalently. Additionally, the Riga plate induced Lorentz power that corresponded to the surface and caused additional surface strain, leading to a rise in the fluid's speed.

The impact of the dimensional parameter Λ on the velocity profile $f'(\Upsilon)$ is illustrated in Fig. 5. It is experienced that the profile $f'(\Upsilon)$ is decaying for enhancing values of the parameter Λ . It is because the thickness of the boundary layer deteriorates as the parameter Λ improves, so the velocity reduces within the boundary layer.

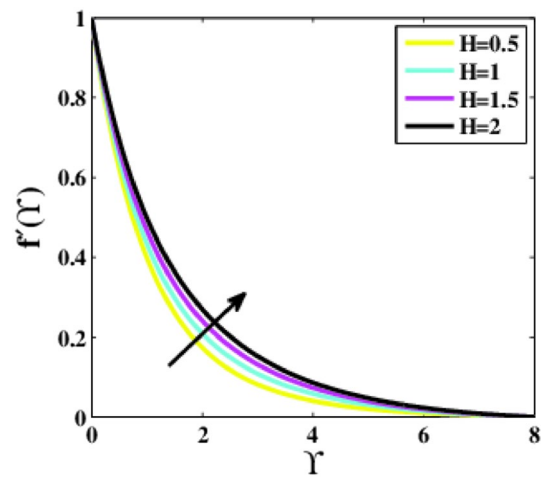


Figure 3. Plots of $f'(\Upsilon)$ for H .

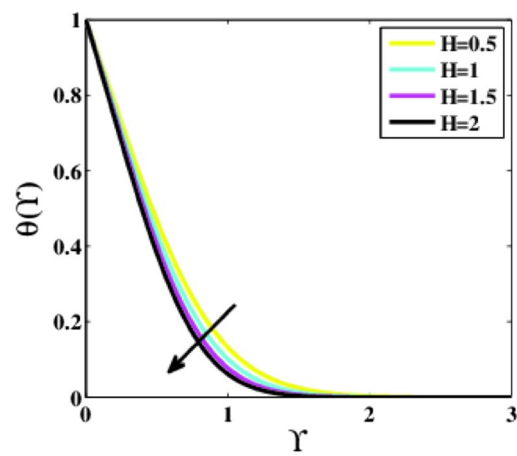


Figure 4. Plots of $\theta(\Upsilon)$ for H .

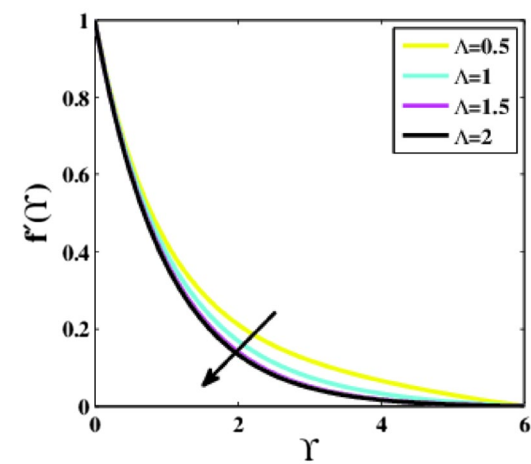


Figure 5. Plots of $f'(\Upsilon)$ for Λ .

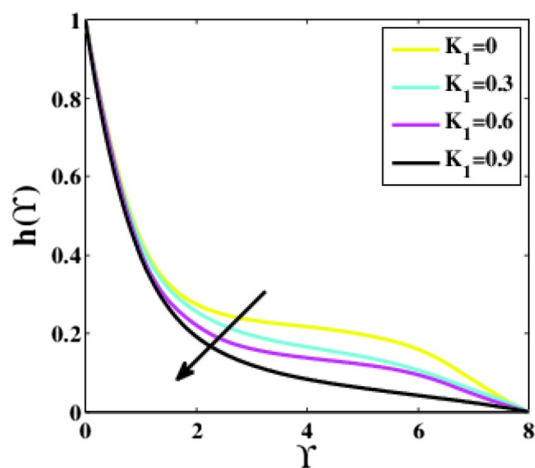


Figure 6. Plots of $h(\gamma)$ for K_1 .

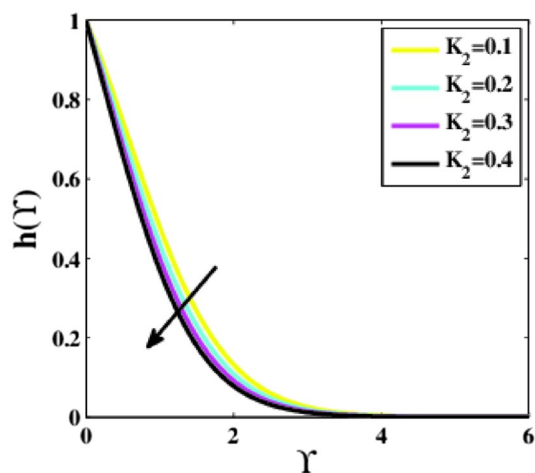


Figure 7. Plots of $h(\gamma)$ for K_2 .

The impacts of the homogeneous and heterogeneous chemical parameters (K_1, K_2) on the profile $h(\gamma)$ are captured in Figs. 6, 7. It is examined that the profile $h(\gamma)$ reduces for higher estimations of both parameters. With escalated values of the parameters K_1, K_2 the reactants are consumed, which is responsible for the reduction in the profile $h(\gamma)$ and boundary layer.

Also, Fig. 8 portrays that upon mounting the Schmidt number Sc , the profile $h(\gamma)$ grows. Since the Schmidt number is defined as the ratio of momentum to mass diffusivity. Therefore, the parameter Sc is increased by large momentum diffusivity relative to mass diffusivity. It finally results in a higher profile $h(\gamma)$.

Figure 9 shows that the velocity profile is observed decaying for the various alterations in the viscoelastic parameter. As the parameter α surges, a noticeable decrement in profile $f'(\gamma)$ is seen. It is because the tensile stress produced by the viscoelastic parameter causes the thickness of the boundary layer to drop and compares transversely, lowering the velocity.

Figure 10 portrays the impression of the magnetic parameter M on the dimensionless velocity profile $f'(\gamma)$ along γ . With rising values of the parameter M , the flow velocity profile is observed to decrease noticeably over the fluid domain. When a magnetic field is applied to a fluid that is electrically conducting, it creates a drag-like force known as Lorentzian force. This force produces friction in the direction of the fluid, and as a result, the fluid velocity decays. The velocity is maximum when $M = 0.1$, but when M rises, the velocity profile decreases.

Figure 11 is drawn to analyze the influence of the Rayleigh number Nc on the non-dimensional velocity profile $f'(\gamma)$. A noticeable increment in the velocity profile is seen for higher estimations of the parameter Nc . For $Nc = 1.0$ the velocity has obtained its maximum value than from the other estimations of Nc .

Figure 12 measures the effectiveness of the mixed convection parameter λ on the dimensionless velocity profile $f'(\gamma)$ along the dimensionless similarity variable γ . A considerable decrement in the profile is seen. A large difference is observed in the decrement of the fluid velocity profile for $\lambda = 4$ from $\lambda = 1.0, 2.0$, and 3.0 .

Figure 13 predicts the influence of the Buoyancy ratio parameter Nr on the non-dimensional profile of the velocity $f'(\gamma)$ alongside γ . The profile $f'(\gamma)$ decreases for larger Nr . The occurrence of nanoparticles increases

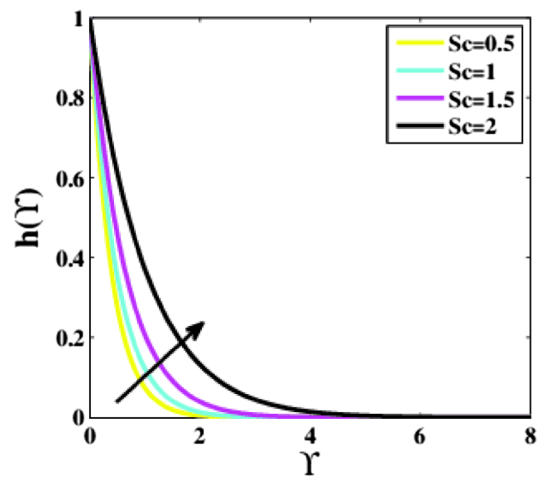


Figure 8. Plots of $h(\Upsilon)$ for Sc .

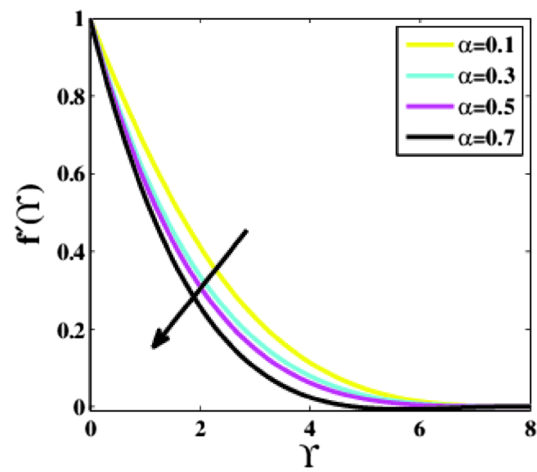


Figure 9. Plots of $f'(\Upsilon)$ for α .

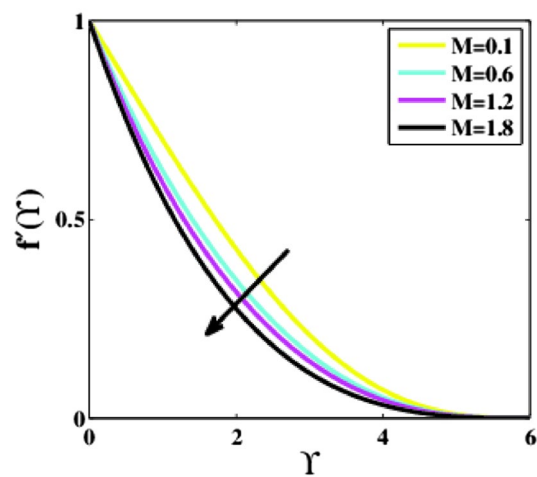


Figure 10. Plots of $f'(\Upsilon)$ for M .

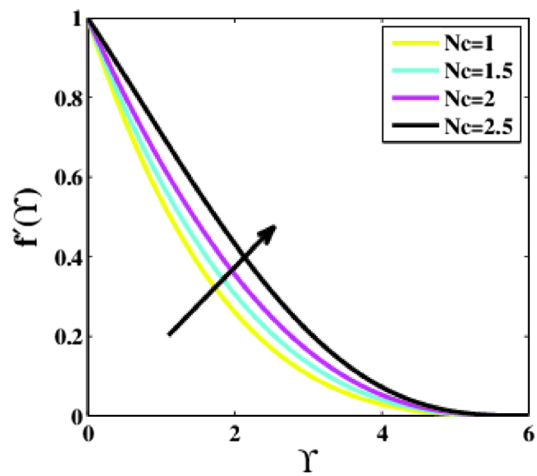


Figure 11. Plots of $f'(\Upsilon)$ for Nc .

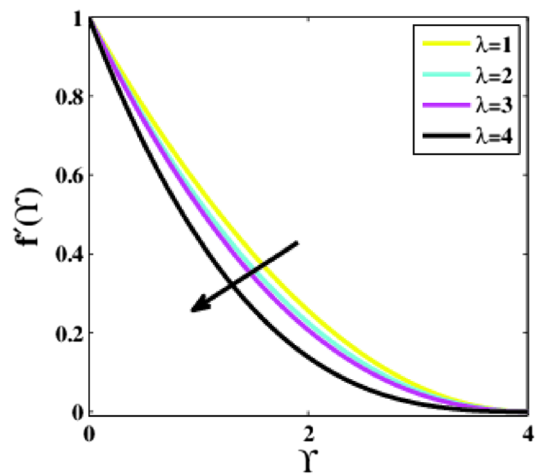


Figure 12. Plots of $f'(\Upsilon)$ for λ .

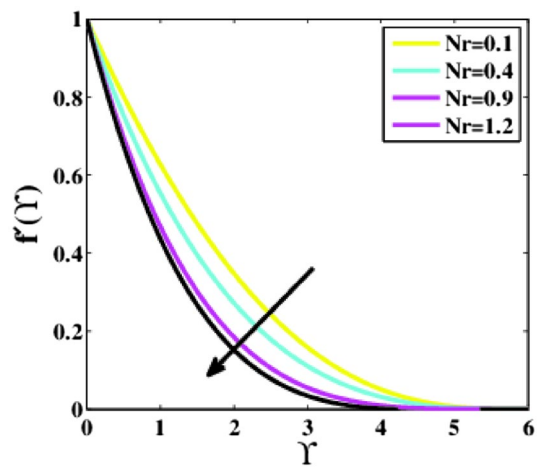


Figure 13. Plots of $f'(\Upsilon)$ for Nr .

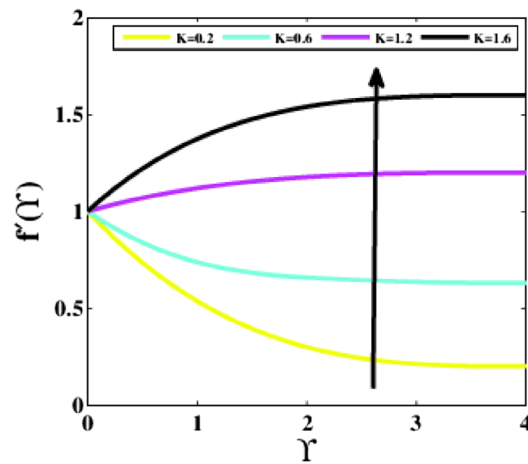


Figure 14. Plots of $f'(\Upsilon)$ for K .

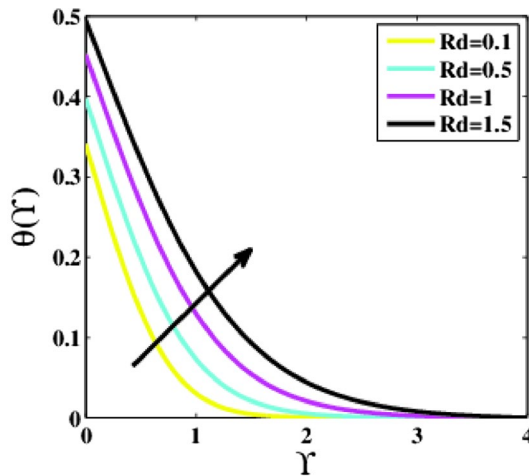


Figure 15. Plots of $\theta(\Upsilon)$ for Rd .

the opposing buoyancy, causing the fluid velocity to diminish. Also, the effects for $Nr = 1.2$ are smaller as compared to $Nr = 0.1, 0.4,$ and 0.9 .

Figure 14 signifies the impression of the velocity ratio parameter K on the non-dimensional velocity distribution $f'(\Upsilon)$. An immense fluctuation in the fluid velocity and the corresponding thickness of the boundary layer is experienced at the points where free stream velocity differs from the Riga plate's velocity. As the velocity ratio parameter increases, the velocity rises, and the thickness of the boundary layer falls.

Figure 15 depicts the temperature profile $\theta(\Upsilon)$ for various values of the radiation parameter Rd . A reasonable increment in temperature profile is observed for growing values of the parameter Rd . The radiation parameter Rd specifies how much conduction heat transfer contributes to thermal radiation transfer. Thus it is self-evident that raising the parameter Rd rises the temperature inside the boundary layer. Because escalation in Rd means a reduction in the co-efficient of mean absorption, which delivers additional heat towards flow, and as a result, an increase in the temperature profile is noticed.

Figure 16 depicts the impact of the Prandtl number Pr on the non-dimensional temperature profile $\theta(\Upsilon)$. The numerical values of the parameter Pr reveal that rising the Prandtl number influences lowering the temperature. A rise in the Prandtl number causes the thickness of the thermal boundary layer to decrease and the average temperature inside the boundary layer to fall. The idea for this is that lower Pr values equate to greater thermal conductivities, allowing heat to escape away from the warmed surface more quickly than with larger Pr values. As a result, the boundary layer becomes thicker for fewer Prandtl numbers, and the heat transfer rate decreases.

Figure 17 aims to present the impact of the variation in the Biot number of heat γ_1 on the non-dimensional temperature profile $\theta(\Upsilon)$. The profile is witnessed escalating for growing values of the Biot number. Because the Biot number and coefficient of heat transmission are inextricably related. As the parameter γ_1 grows, the fluid conductivity decays, but the heat transmission coefficient rises, raising the fluid's temperature.

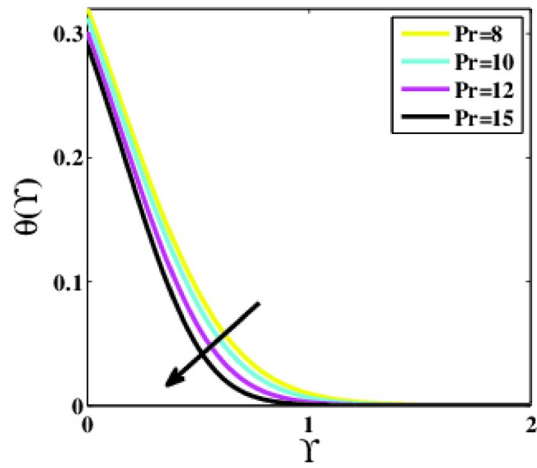


Figure 16. Plots of $\theta(\Upsilon)$ for Pr .

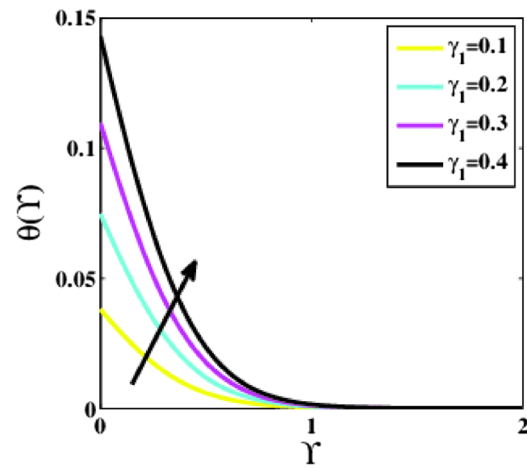


Figure 17. Plots of $\theta(\Upsilon)$ for γ_1 .

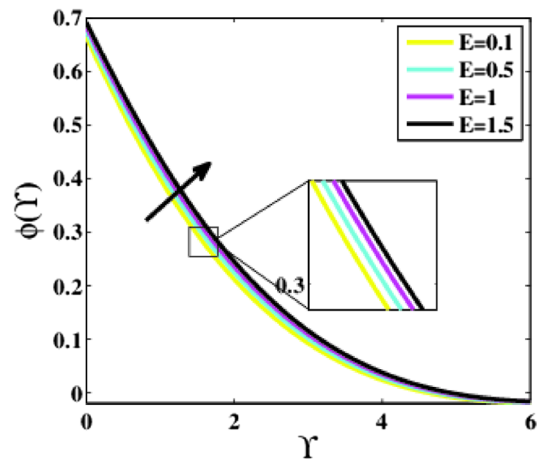


Figure 18. Plots of $\phi(\Upsilon)$ for E .

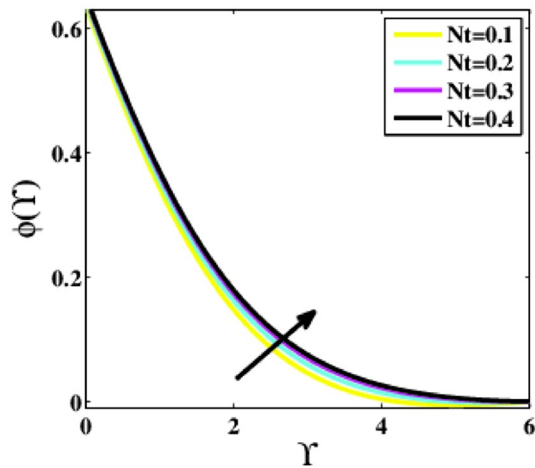


Figure 19. Plots of $\phi(\Upsilon)$ for Nt .

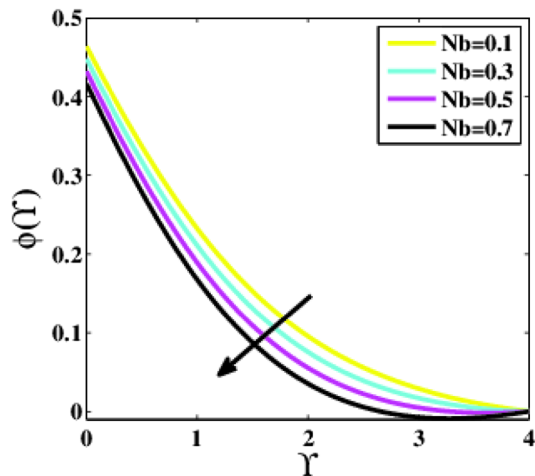


Figure 20. Plots of $\phi(\Upsilon)$ for Nb .

Figure 18 demonstrates the effects of the activation energy parameter E on the concentration profile $\phi(\zeta)$. The rise in the parameter E leads to an increase in the profile $\phi(\Upsilon)$. The deterioration of the modified Arrhenius function is caused by increasing E . Eventually, this encourages productive chemical processes, resulting in increased concentration. The term $\phi \exp\left(\frac{-E}{1+\mu\theta}\right)$ in the Eq. (11) is a more useful tool for determining how Arrhenius activation influences nanoparticle concentration.

Figure 19, 20 are extracted to predict the effects of the thermophoresis and Brownian motion parameters (Nt , Nb). For varying values of the parameters Nt and Nb , the profile $\phi(\Upsilon)$ explores two possible patterns. As the parameter Nt rises, the profile $\phi(\Upsilon)$ in Fig. 19 rises as well because nanoparticles are distributed from the hot to the ambient fluid during the thermophoresis process, and as a result, nanoparticle concentration augments. Whereas the concentration in Fig. 20 diminishes as the Brownian motion parameter rises. The Brownian motion is created by nanoparticles colliding with a base fluid. The arbitrary motion of nanoparticles increases the kinetic energy unless the Brownian motion has a major influence on nanoparticle diffusion.

Figure 21 interprets the impact of the Lewis number Le on the non-dimensional concentration profile $\phi(\Upsilon)$. Clearly, the profile $\phi(\Upsilon)$ reduces as the parameter Le enhances. Lewis number denotes the relative contribution of the thermal to the species diffusion rate within the boundary layer region. According to the definition, the parameter Le is basically the ratio of Schmidt to Prandtl number. As a result, when $Le = 1.0$, heat and species disperse at equal speed. When $Le > 1.0$, heat diffuses more quickly than species. The boundary layer of species nanoparticle concentration grows steeper when the Lewis number is enhanced.

Figure 22 elucidates the impression of the Biot number of solution γ_2 on the dimensionless concentration profile $\phi(\Upsilon)$. It has been observed that as the parameter γ_2 increases the profile $\phi(\Upsilon)$ increases. According to the definition of the Biot number, the transferred mass will be spread throughout the surface by convection. As a result, the profile of nanoparticle concentration is amplified.

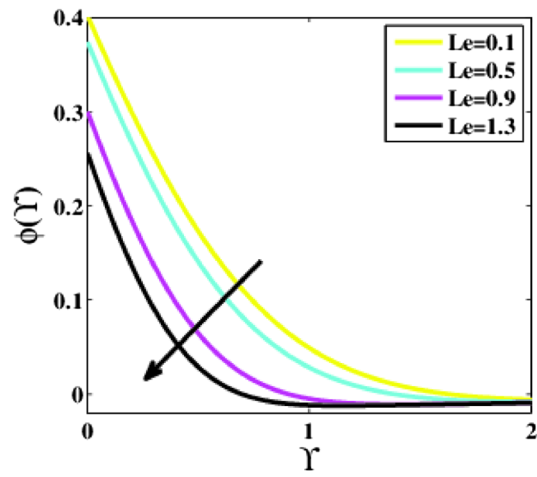


Figure 21. Plots of $\phi(\Upsilon)$ for Le .

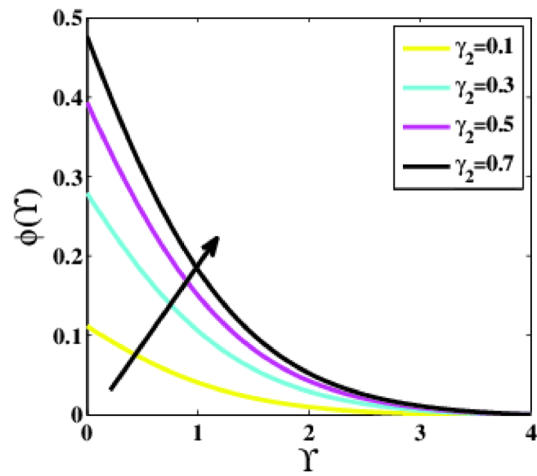


Figure 22. Plots of $\phi(\Upsilon)$ for γ_2 .

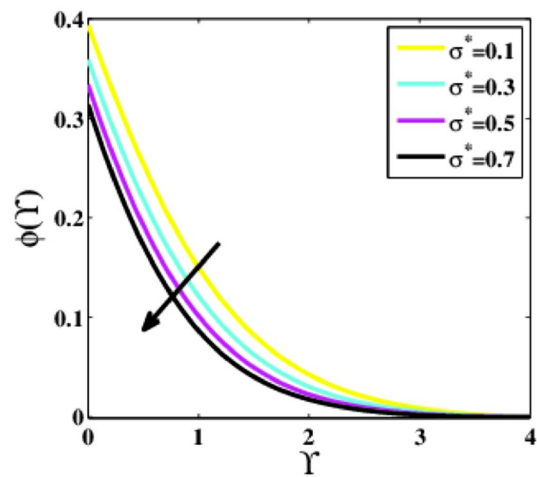


Figure 23. Plots of $\phi(\Upsilon)$ for σ^* .

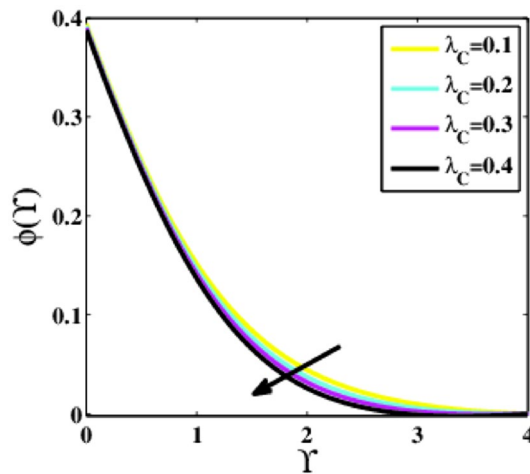


Figure 24. Plots of $\phi(\Upsilon)$ for λ_C .

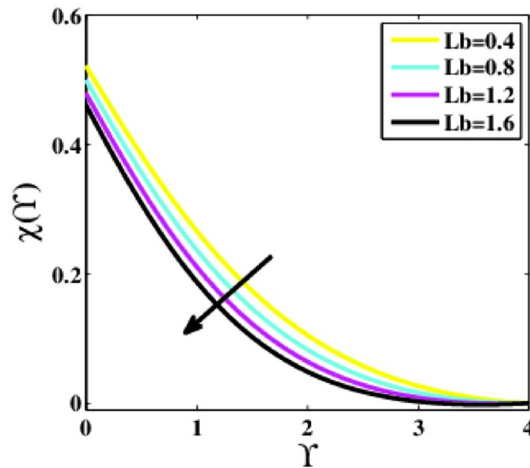


Figure 25. Plots of $\chi(\Upsilon)$ for Lb .

Figure 23 captures the impression of the chemical reaction factor σ^* on the concentration profile $\phi(\Upsilon)$. The profile $\phi(\Upsilon)$ is decreasing for growing values of the parameter σ^* . When the parameter σ^* increases, the number of solute molecules involved in the reaction increases, lowering the concentration. As a result of the destructive chemical reaction, the solutal boundary layer's thickness is considerably reduced.

Figure 24 indicates the effects of the relaxation time of the mass parameter λ_C upon the dimensionless concentration profile $\phi(\Upsilon)$. The profile $\phi(\Upsilon)$ reduces as the parameter λ_C surges. It is because if the parameter λ_C is larger, then the particles of the fluid will take longer to disperse, resulting in a decrease in the concentration profile.

Figure 25 is plotted to predict the effects of the bio-convection Lewis number Lb upon the dimensionless profile of microorganisms $\chi(\Upsilon)$. It is noticed that the profile $\chi(\Upsilon)$ observe to decrease for higher Lb . Physically, the parameter Lb is inversely proportional to the thermal diffusivity; raising Lb lessens the thermal diffusivity, resulting in a decrease in the motile density of microorganisms.

Figure 26 is delineated to determine the effects of the Peclet number Pe on the non-dimensional microorganisms profile $\chi(\Upsilon)$. It is perceived that the profile $\chi(\Upsilon)$ is decaying for greater estimations of the parameter Pe . Physically, the parameter Pe is inversely linked with the diffusivity of the microorganisms and has a direct association with cell swimming speed. Consequently, an increase in Pe increases cell swimming speed while reducing microbe diffusivity. As a result, the microorganism's ability to develop Pe is reduced.

Figure 27 demonstrates the impression of the Biot number of microorganisms γ_3 on the non-dimensional profile of the microorganisms $\chi(\Upsilon)$. The profile $\chi(\Upsilon)$ escalates for rising values of the parameter γ_3 . A dramatic increase from $\gamma_3 = 0.1$ to $\gamma_3 = 0.2$ is noticed.

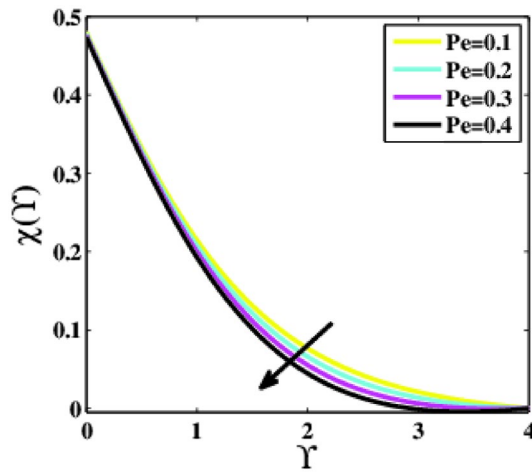


Figure 26. Plots of $\chi(\Upsilon)$ for Pe .

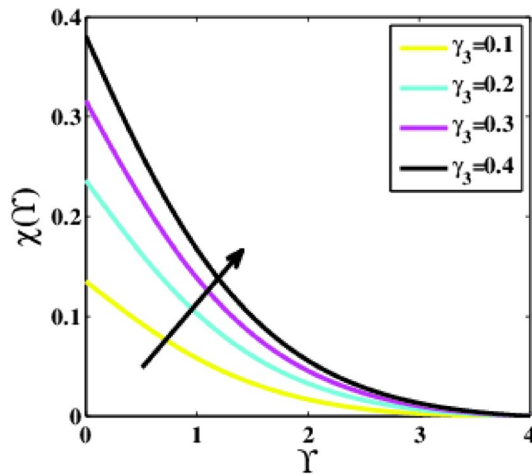


Figure 27. Plots of $\chi(\Upsilon)$ for γ_3 .

Table discussion

The physically interesting quantities like Nusselt number $N_u Re_x^{-\frac{1}{2}}$, Sherwood number $Sh_x Re_x^{-\frac{1}{2}}$, and local density number $Nn_x Re_x^{-\frac{1}{2}}$ are numerically calculated in Table 2 for diverse ranges of the dimensionless parameters like $\alpha, \lambda, Rd, E, K, Nt, Nb, Lb, H, \Lambda$ and Le .

Conclusion

A theoretical analysis has been carried out to describes the characteristics of bioconvection and gyrotactic microorganisms in the MHD flow of Walters-B fluid with homogenous and heterogeneous chemical reactions over a Riga plate. The Buongiorno nanofluid model has been used to model the flow dynamics in terms of highly nonlinear PDEs, which are later transmuted into mixed ODEs with suitable similarity variables. The resultant ODEs are tackled through the assistance of the efficient Galerkin finite element method in COMSOL software. Thus following concluding remarks are drawn from the present analysis:

- The velocity increases for the parameters N and K but is effectively controlled for the parameters $H, \Lambda, \alpha, M, \lambda,$ and Nr .
- The temperature escalates for the parameters $Rd,$ and γ_1 whereas it decays for the parameters Pr .
- The concentration of nanoparticles augments for the parameters E, Nt and γ_2 but it falls short for the parameters Nb, Le, σ^* and λ_C .
- The gyrotactic microorganisms boosted for the parameter γ_3 however, it reduces for the parameters Lb and Pe .

λ	α	E	Rd	K	Nb	Nt	Lb	H	Λ	Le	$Nu_x Re_x^{-1}$	$Sh_x Re_x^{-1}$	$Nt_x Re_x^{-1}$
1	1	0.1	0.1	1.1	0.3	0.1	0.4	0.2	0.2	0.5	0.35441	0.29157	0.27379
2											0.33520	0.24121	0.24363
3											0.31624	0.23833	0.22364
	1.0										0.35441	0.29157	0.27379
	0.5										0.31935	0.27364	0.23027
	0.7										0.27162	0.24851	0.21343
		0.1									0.35441	0.29157	0.27379
		0.5									0.38462	0.26493	0.23736
		1									0.40249	0.24436	0.20804
			0.1								0.35441	0.29157	0.27379
			0.5								0.31827	0.32611	0.27379
			1.0								0.28726	0.35923	0.27379
				1.1							0.35441	0.29157	0.27379
				1.2							0.33319	0.31169	0.29849
				1.3							0.30258	0.33113	0.31064
					0.1						0.35441	0.29157	0.27379
					0.3						0.30582	0.34165	0.30862
					0.5						0.25780	0.38861	0.34874
						0.1					0.40663	0.34529	0.31724
						0.2					0.37331	0.32026	0.29136
						0.4					0.35441	0.29157	0.27379
							0.4				0.35441	0.29157	0.27379
							0.8				0.35441	0.29157	0.30412
							1.2				0.35441	0.29157	0.34960
								0.2			0.35441	0.29157	0.27379
								1			0.37545	0.31945	0.30772
								1.5			0.40198	0.33602	0.32159
									0.2		0.35441	0.29157	0.27379
									1		0.38299	0.32169	0.29892
									1.5		0.42102	0.34472	0.31869
										0.1	0.30223	0.27854	0.23857
										0.5	0.35441	0.29157	0.27379
										0.9	0.39964	0.35359	0.29265

Table 2. Nusselt, Sherwood quantities and consistency amount at the stretching walls.

The Galerkin-finite element method could be applied to a variety of physical and technical challenges in the future^{72–83}. Some recent developments exploring the significance of the considered research domain are reported in the studies^{84–93}.

Data availability

All data generated or analyzed during this study are included in this published article.

Received: 11 June 2022; Accepted: 4 October 2022

Published online: 27 October 2022

References

- Gupta, S. K., Gupta, S., Gupta, T., Raghav, A. & Singh, A. A review on recent advances and applications of nanofluids in plate heat exchanger. *Mater. Today: Proc.* **44**, 229–241 (2021).
- Salilih, E. M. *et al.* Annual performance analysis of small scale industrial waste heat assisted solar tower power plant and application of nanofluid. *J. Taiwan Inst. Chem. Eng.* **124**, 216–227 (2021).
- Olabi, A. G. *et al.* Application of nanofluids for enhanced waste heat recovery: A review. *Nano Energy* **84**, 105871 (2021).
- Wang, X. *et al.* A comprehensive review on the application of nanofluid in heat pipe based on the machine learning: Theory, application and prediction. *Renew. Sustain. Energy Rev.* **150**, 111434 (2021).
- Souza, R. R. *et al.* Recent advances on the thermal properties and applications of nanofluids: From nanomedicine to renewable energies. *Appl. Therm. Eng.* **201**, 117725 (2022).
- Nugroho, A. *et al.* Extensive examination of sonication duration impact on stability of Al₂O₃-Polyol ester nanolubricant. *Int. Commun. Heat Mass Transfer* **126**, 105418 (2021).
- Reddy, J. V. R., Sugunamma, V. & Sandeep, N. Enhanced heat transfer in the flow of dissipative non-Newtonian Casson fluid flow over a convectively heated upper surface of a paraboloid of revolution. *J. Mol. Liquids* **229**, 380–388 (2017).

8. Walters, K. J. Non-Newtonian effects in some elasto-viscous liquids whose behaviour at small rates of shear is characterized by a general linear equation of state. *Q. J. Mech. Appl. Math.* **15**(1), 63–76 (1962).
9. Chu, Y.-M. *et al.* Thermophoresis particle deposition analysis for nonlinear thermally developed flow of Magneto-Walter's B nanofluid with buoyancy forces. *Alex. Eng. J.* **60**(1), 1851–1860 (2021).
10. Waqas, H., Khan, S. U., Khan, M. I., Alzahrani, F. & Qayyum, S. Study of homogeneous–heterogeneous reactions in bioconvection stagnation point slip flow of Walter's-B nanofluid with nonlinear thermal radiation and activation energy. *Int. Commun. Heat Mass Transf* **129**, 105729 (2021).
11. Siddique, I., Shah, N. A. & Abro, K. A. Thermography of ferromagnetic Walter's-B fluid through varying thermal stratification. *S. Afr. J. Chem. Eng.* **36**, 118–126 (2021).
12. Awasthi, M., Dharamendra, K. & Yadav, D. Stability characteristics of Walter's B viscoelastic fluid in a cylindrical configuration with heat transfer. *Proc. Inst. Mech. Eng. Part E J. Process Mech. Eng.* **236**, 10370–10377 (2022).
13. Ahmad, L. *et al.* Non-axisymmetric Homann stagnation-point flow of unsteady Walter's B nanofluid over a vertical cylindrical disk. *Proc. Inst. Mech. Eng. Part E J. Process Mech. Eng.* <https://doi.org/10.1177/09544089211064480> (2021).
14. Sunthrayuth, P., Alderremy, A., Aly, S., Shah, R. & Akgül, A. Exact analysis of electro-osmotic flow of Walters'-B fluid with non-singular kernel. *Pramana* **95**(4), 1–10 (2021).
15. Ahmad, M., Shehzad, S. A., Malik, J. & Taj, M. Stagnation point Walter'sB nanofluid flow over power-law lubricating surface with slip conditions: Hybrid HAM solutions. *Proc. Inst. Mech. Eng. C J. Mech. Eng. Sci.* **235**(19), 4002–4013 (2021).
16. Idowu, A. S. & Falodun, B. O. Soret–Dufour effects on MHD heat and mass transfer of Walter'sB viscoelastic fluid over a semi-infinite vertical plate: Spectral relaxation analysis. *J. Taibah Univ. Sci.* **13**(1), 49–62 (2019).
17. Rana, P., Shukla, N., Gupta, Y. & Pop, I. Analytical prediction of multiple solutions for MHD Jeffery-Hamel flow and transfer utilizing KKL nanofluid model. *Phys. Lett. A* **383**, 176–185 (2019).
18. Mahanthesh, B., Thriveni, K., Rana, P. & Muhammad, T. Radiative heat transfer of nanomaterial on a convectively heated circular tube with activation energy and nanoparticle aggregation kinematic effects. *Int. Commun. Heat Mass Transf* **127**, 105568 (2021).
19. Rana, P., Gupta, S. & Gupta, G. Unsteady nonlinear thermal convection flow of MWCNT-MgO/EG hybrid nanofluid in the stagnation-point region of a rotating sphere with quadratic thermal radiation: RSM for optimization. *Int. Commun. Heat Mass Transf* **134**, 106025 (2022).
20. Rana, P., Gupta, S., Pop, I. & Gupta, G. Three-dimensional heat transfer of 29 nm CuO-H₂O nanofluid with Joule heating and slip effects over a wedge surface. *Int. Commun. Heat Mass Transf* **134**, 106001 (2022).
21. Rana, P., Kumar, A. & Gupta, G. Impact of different arrangements of heated elliptical body, fins and differential heater in MHD convective transport phenomena of inclined cavity utilizing hybrid nanofluid: Artificial neural network prediction. *Int. Commun. Heat Mass Transf* **132**, 105900 (2022).
22. Rana, P. & Gupta, G. Heat transfer optimization of Marangoni convective flow of nanofluid over an infinite disk with Stefan blowing and slip effects using Taguchi method. *Int. Commun. Heat Mass Transf* **130**, 105822 (2022).
23. Sheikholeslami, M. & Ebrahimpour, Z. Thermal improvement of linear Fresnel solar system utilizing Al₂O₃-water nanofluid and multi-way twisted tape. *Int. J. Therm. Sci.* **176**, 107505 (2022).
24. Sheikholeslami, M., Said, Z. & Jafaryar, M. Hydrothermal analysis for a parabolic solar unit with wavy absorber pipe and nanofluid. *Renew. Energy* **188**, 922–932 (2022).
25. Sheikholeslami, M., Jafaryar, M., Barzegar-Gerdroodbary, M. & Alavi, A. H. Influence of novel turbulator on efficiency of solar collector system. *Environ. Technol. Innov.* **26**, 102383 (2022).
26. Sheikholeslami, M. & Farshad, S. A. Nanoparticles transportation with turbulent regime through a solar collector with helical tapes. *Adv. Powder Technol.* **33**(3), 103510 (2022).
27. Akolade, M. T. & Tijani, Y. O. A comparative study of three dimensional flow of Casson-Williamson nanofluids past a riga plate: Spectral quasi-linearization approach. *Part. Differ. Equ. Appl. Math.* **4**, 100108 (2021).
28. Hakeem, A. K., Ragupathi, P., Ganga, B. & Nadeem, S. Three-dimensional viscous dissipative flow of nanofluids over a Riga plate. *J. Heat Mass Transfer Res.* **8**(1), 49–60 (2021).
29. Rawat, S. K., Mishra, A. & Kumar, M. Numerical study of thermal radiation and suction effects on copper and silver water nanofluids past a vertical Riga plate. *Multidiscipl. Model. Mater. Struct.* **15**, 714–736 (2019).
30. Rasool, G. & Zhang, T. Characteristics of chemical reaction and convective boundary conditions in Powell-Eyring nanofluid flow along a radiative Riga plate. *Heliyon* **5**(4), e01479 (2019).
31. Asogwa, K. K., Mebarek-Oudina, F. & Animasaun, I. L. Comparative investigation of water-based Al₂O₃ nanoparticles through water-based CuO nanoparticles over an exponentially accelerated radiative Riga plate surface via heat transport. *Arab. J. Sci. Eng.* **2022**, 1–18 (2022).
32. Anuar, N. S., Bachok, N. & Pop, I. Cu-Al₂O₃/water hybrid nanofluid stagnation point flow past MHD stretching/shrinking sheet in presence of homogeneous–heterogeneous and convective boundary conditions. *Mathematics* **8**(8), 1237 (2020).
33. Mishra, S. R., Mathur, P. & Ali, H. M. Analysis of homogeneous–heterogeneous reactions in a micropolar nanofluid past a nonlinear stretching surface: Semi-analytical approach. *J. Therm. Anal. Calorim.* **144**(6), 2247–2257 (2021).
34. Almutairi, F., Khaled, S. M. & Ebaied, A. MHD flow of nanofluid with homogeneous–heterogeneous reactions in a porous medium under the influence of second-order velocity slip. *Mathematics* **7**(3), 220 (2019).
35. Li, Y.-X., Sumaira, Q., Khan, M. I., Elmasry, Y. & Chu, Y.-M. Motion of hybrid nanofluid (MnZnFe₂O₄–NiZnFe₂O₄–H₂O) with homogeneous–heterogeneous reaction: Marangoni convection. *Math. Comput. Simul.* **190**, 1379–1391 (2021).
36. Raees, A., Wang, R. Z. & Xu, H. A homogeneous–heterogeneous model for mixed convection in gravity-driven film flow of nanofluids. *Int. Commun. Heat Mass Transfer* **95**, 19–24 (2018).
37. Waqas, H., Hussain, M., Alqarni, M. S., Eid, M. R. & Muhammad, T. Numerical simulation for magnetic dipole in bioconvection flow of Jeffrey nanofluid with swimming motile microorganisms. *Waves Random Complex Media* **2021**, 1–18 (2021).
38. Waqas, H., Imran, M. & Bhatti, M. M. Influence of bioconvection on Maxwell nanofluid flow with the swimming of motile microorganisms over a vertical rotating cylinder. *Chin. J. Phys.* **68**, 558–577 (2020).
39. Waqas, H., Farooq, U., Khan, S. A., Alshehri, H. M. & Goodarzi, M. Numerical analysis of dual variable of conductivity in bioconvection flow of Carreau-Yasuda nanofluid containing gyrotactic motile microorganisms over a porous medium. *J. Therm. Anal. Calorim.* **145**(4), 2033–2044 (2021).
40. Waqas, H., Naseem, R., Muhammad, T. & Farooq, U. Bioconvection flow of Casson nanofluid by rotating disk with motile microorganisms. *J. Market. Res.* **13**, 2392–2407 (2021).
41. Waqas, H., Imran, M., Muhammad, T., Sait, S. M. & Ellahi, R. Numerical investigation on bioconvection flow of Oldroyd-B nanofluid with nonlinear thermal radiation and motile microorganisms over rotating disk. *J. Therm. Anal. Calorim.* **145**(2), 523–539 (2021).
42. Waqas, H., Khan, S. U., Hassan, M., Bhatti, M. M. & Imran, M. Analysis on the bioconvection flow of modified second-grade nanofluid containing gyrotactic microorganisms and nanoparticles. *J. Mol. Liq.* **291**, 111231 (2019).
43. Waqas, H., Khan, S. U., Imran, M. & Bhatti, M. M. Thermally developed Falkner-Skan bioconvection flow of a magnetized nanofluid in the presence of a motile gyrotactic microorganism: Buongiorno's nanofluid model. *Phys. Scr.* **94**(11), 115304 (2019).
44. Bég, O. A., Prasad, V. R. & Vasu, B. Numerical study of mixed bioconvection in porous media saturated with nanofluid containing oxytactic microorganisms. *J. Mech. Med. Biol.* **13**(04), 1350067 (2013).

45. Sajid, T., Sagheer, M., Hussain, S. & Shahzad, F. Impact of double-diffusive convection and motile gyrotactic microorganisms on magnetohydrodynamics bioconvection tangent hyperbolic nanofluid. *Open Phys.* **18**(1), 74–88 (2020).
46. Waqas, H., Manzoor, U., Alqarni, M. S. & Muhammad, T. Numerical study for bioconvection in magnetized flow of micropolar nanofluid utilizing gyrotactic motile microorganisms. *Waves Random Complex Media* **2021**, 1–16 (2021).
47. Khan, S. U., Rauf, A., Shehzad, S. A., Abbas, Z. & Javed, T. Study of bioconvection flow in Oldroyd-B nanofluid with motile organisms and effective Prandtl approach. *Phys. A* **527**, 121179 (2019).
48. Imran, M., Farooq, U., Waqas, H., Anqi, A. E. & Safaei, M. R. Numerical performance of thermal conductivity in Bioconvection flow of cross nanofluid containing swimming microorganisms over a cylinder with melting phenomenon. *Case Stud. Therm. Eng.* **26**, 101181 (2021).
49. Muhammad, T., Waqas, H., Manzoor, U., Farooq, U. & Rizvi, Z. F. On doubly stratified bioconvective transport of Jeffrey nanofluid with gyrotactic motile microorganisms. *Alex. Eng. J.* **61**(2), 1571–1583 (2022).
50. Rao, M., Gangadhar, K., Chamkha, A. J. & Surekha, P. Bioconvection in a convective nanofluid flow containing gyrotactic microorganisms over an isothermal vertical cone embedded in a porous surface with chemical reactive species. *Arab. J. Sci. Eng.* **46**(3), 2493–2503 (2021).
51. Sheikholeslami, M. Numerical investigation of solar system equipped with innovative turbulator and hybrid nanofluid. *Sol. Energy Mater. Sol. Cells* **243**, 111786 (2022).
52. Sheikholeslami, M. Analyzing melting process of paraffin through the heat storage with honeycomb configuration utilizing nanoparticles. *J. Energy Storage* **52**, 104954 (2022).
53. Sheikholeslami, M. Numerical analysis of solar energy storage within a double pipe utilizing nanoparticles for expedition of melting. *Sol. Energy Mater. Sol. Cells* **245**, 111856 (2022).
54. Sheikholeslami, M. & Ebrahimpour, Z. Nanofluid performance in a solar LFR system involving turbulator applying numerical simulation. *Adv. Powder Technol.* **33**(8), 103669 (2022).
55. Ahmed, S. E. FEM-CBS algorithm for convective transport of nanofluids in inclined enclosures filled with anisotropic non-Darcy porous media using LTNEM. *Int. J. Numer. Methods Heat Fluid Flow* **31**, 570–594 (2020).
56. Hiba, B. *et al.* A novel case study of thermal and streamline analysis in a grooved enclosure filled with (Ag–MgO/Water) hybrid nanofluid: Galerkin FEM. *Case Stud. Therm. Eng.* **28**, 101372 (2021).
57. Ali, L., Ali, B. & Ghori, M. B. Melting effect on Cattaneo-Christov and thermal radiation features for aligned MHD nanofluid flow comprising microorganisms to leading edge: FEM approach. *Comput. Math. Appl.* **109**, 260–269 (2022).
58. Abderrahmane, A. I. S. A. *et al.* Non-Newtonian nanofluid natural convective heat transfer in an inclined Half-annulus porous enclosure using FEM. *Alex. Eng. J.* **61**(7), 5441–5453 (2022).
59. Rana, P. & Gupta, G. FEM Solution to quadratic convective and radiative flow of Ag-MgO/H₂O hybrid nanofluid over a rotating cone with Hall current: Optimization using response surface methodology. *Math. Comput. Simul.* **201**, 121–141 (2022).
60. Pasha, P. & Domiri-Ganji, D. Hybrid analysis of micropolar ethylene-glycol nanofluid on stretching surface mounted triangular, rectangular and chamfer fins by FEM strategy and optimization with RSM method. *Int. J. Eng.* **35**(5), 845–854 (2022).
61. Redouane, F. *et al.* Heat flow saturate of Ag/MgO-water hybrid nanofluid in heated trigonal enclosure with rotate cylindrical cavity by using Galerkin finite element. *Sci. Rep.* **12**(1), 1–20 (2022).
62. Alrowaili, D., Ahmed, S. E., Elshehaby, H. M. & Ezzeldien, M. Magnetic radiative buoyancy-driven convection of MWCNTs-C₂H₆O₂ power-law nanofluids in inclined enclosures with wavy walls. *Alex. Eng. J.* **61**(11), 8677–8686 (2022).
63. Zaaroura, I. *et al.* Modeling and prediction of the dynamic viscosity of nanofluids by a homogenization method. *Braz. J. Phys.* **51**(4), 1136–1144 (2021).
64. Ahmed, S. E. & Alhazmi, M. Impacts of the rotation and various thermal conditions of cylinders within lid-driven enclosures filled with glass balls in the presence of radiation: FEM simulation. *Int. Commun. Heat Mass Transfer* **128**, 105603 (2021).
65. Madani, T., Ali, S., Abkar, R. & Khoelrar, R. On the study of viscoelastic Walters' B fluid in boundary layer flows. *Math. Probl. Eng.* **2012**, 1–8 (2012).
66. Wakif, A., Animasaun, I. L., Khan, U. & Alshehri, A.M. Insights into the generalized Fourier's and Fick's laws for simulating mixed bioconvective flows of radiative-reactive walters-B fluids conveying tiny particles subject to Lorentz force. (2021).
67. Alshomrani, A. S. On generalized Fourier's and Fick's laws in bio-convection flow of magnetized burgers' nanofluid utilizing motile microorganisms. *Mathematics* **8**(7), 1186 (2020).
68. Khan, M. I., Alzahrani, F. & Hobiny, A. Heat transport and nonlinear mixed convective nanomaterial slip flow of Walter-B fluid containing gyrotactic microorganisms. *Alex. Eng. J.* **59**(3), 1761–1769 (2020).
69. Das, S., Chakraborty, S., Jana, R. N. & Makinde, O. D. Entropy analysis of unsteady magneto-nanofluid flow past accelerating stretching sheet with convective boundary condition. *Appl. Math. Mech.* **36**(12), 1593–1610 (2015).
70. Qureshi, M. A. A case study of MHD driven Prandtl-Eyring hybrid nanofluid flow over a stretching sheet with thermal jump conditions. *Case Stud. Therm. Eng.* **28**, 101581 (2021).
71. Hussain, S. M. Dynamics of radiative Williamson hybrid nanofluid with entropy generation: Significance in solar aircraft. *Sci. Rep.* **12**(1), 1–23 (2022).
72. Jamshed, W. & Aziz, A. Entropy analysis of TiO₂-Cu/EG Casson hybrid nanofluid via Cattaneo-Christov heat flux model. *Appl. Nanosci.* **08**, 01–14 (2018).
73. Jamshed, W. Numerical investigation of MHD impact on Maxwell nanofluid. *Int. Commun. Heat Mass Transfer* **120**(5), 683 (2021).
74. Jamshed, W. & Nisar, K. S. Computational single phase comparative study of Williamson nanofluid in parabolic trough solar collector via Keller box method. *Int. J. Energy Res.* **45**(7), 10696–10718 (2021).
75. Jamshed, W., Devi, S. U. & Nisar, K. S. Single phase-based study of Ag-Cu/EO Williamson hybrid nanofluid flow over a stretching surface with shape factor. *Phys. Scr.* **96**, 065202 (2021).
76. Jamshed, W., Nisar, K. S., Ibrahim, R. W., Shahzad, F. & Eid, M. R. Thermal expansion optimization in solar aircraft using tangent hyperbolic hybrid nanofluid: A solar thermal application. *J. Mater. Res. Technol.* **14**, 985–1006 (2021).
77. Jamshed, W. *et al.* Computational frame work of Cattaneo-Christov heat flux effects on engine oil based Williamson hybrid nanofluids: A thermal case study. *Case Stud. Therm. Eng.* **26**, 101179 (2021).
78. Jamshed, W. *et al.* Features of entropy optimization on viscous second grade nanofluid streamed with thermal radiation: A Tiwari and Das model. *Case Stud. Therm. Eng.* **27**, 101291 (2021).
79. Jamshed, W. *et al.* Thermal growth in solar water pump using Prandtl-Eyring hybrid nanofluid: A solar energy application. *Sci. Rep.* **11**, 18704 (2021).
80. Jamshed, W. *et al.* Implementing renewable solar energy in presence of Maxwell nanofluid in parabolic trough solar collector: A computational study. *Waves Random Complex Media* **2021**, 1–32 (2021).
81. Jamshed, W. Finite element method in thermal characterization and streamline flow analysis of electromagnetic silver-magnesium oxide nanofluid inside grooved enclosure. *Int. Commun. Heat Mass Transfer* **130**, 105795 (2021).
82. Jamshed, W. *et al.* Thermal characterization of coolant maxwell type nanofluid flowing in parabolic trough solar collector (PTSC) used inside solar powered ship application. *Coatings* **11**(12), 1552 (2021).
83. Jamshed, W. *et al.* Dynamical irreversibility processes analysis of Poiseuille magneto-hybrid nanofluid flow in microchannel: A novel case study. *Waves Random Complex Media* **2022**, 1–23 (2022).
84. Hussain, S. M. *et al.* Effectiveness of nonuniform heat generation (sink) and thermal characterization of a carreau fluid flowing across a nonlinear elongating cylinder: A numerical study. *ACS Omega* **7**, 25309–25320 (2022).

85. Pasha, A. A. *et al.* Statistical analysis of viscous hybridized nanofluid flowing via Galerkin finite element technique. *Int. Commun. Heat Mass Transfer* **137**, 106244 (2022).
86. Hussain, S. M., Jamshed, W., Pasha, A. A., Adil, M. & Akram, M. Galerkin finite element solution for electromagnetic radiative impact on viscid Williamson two-phase nanofluid flow via extendable surface. *Int. Commun. Heat Mass Transfer* **137**, 106243 (2022).
87. Shahzad, F. *et al.* Thermal valuation and entropy inspection of second-grade nanoscale fluid flow over a stretching surface by applying Koo–Kleinstreuer–Li relation. *Nanotechnol. Rev.* **11**, 2061–2077 (2022).
88. Jamshed, W. *et al.* Solar energy optimization in solar-HVAC using Sutterby hybrid nanofluid with Smoluchowski temperature conditions: A solar thermal application. *Sci. Rep.* **12**, 11484 (2022).
89. Akgül, E. K. *et al.* Analysis of respiratory mechanics models with different kernels. *Open Phys.* **20**, 609–615 (2022).
90. Jamshed, W. *et al.* Computational technique of thermal comparative examination of Cu and Au nanoparticles suspended in sodium alginate as Sutterby nanofluid via extending PTSC surface. *J. Appl. Biomater. Funct. Mater.* **20**, 1–20 (2022).
91. Dhange, M. *et al.* A mathematical model of blood flow in a stenosed artery with post-stenotic dilatation and a forced field. *PLoS ONE* **17**, e0266727 (2022).
92. Akram, M. *et al.* Irregular heat source impact on Carreau nanofluid flowing via exponential expanding cylinder: A thermal case study. *Case Stud. Thermal Eng.* **36**, 102190 (2022).
93. Shahzad, F., Jamshed, W., Ahmad, A., Safdar, R. & Alam, M. M. Efficiency evaluation of solar water-pump using nanofluids in parabolic trough solar collector: 2nd order convergent approach waves in random and complex media (2022).

Acknowledgements

The researchers would like to thank the Deanship of Scientific Research, Qassim University for funding the publication of this project.

Author contributions

F.S. and W.J. formulated the problem. F.S., W.J. and U. solved the problem. F.S., W.J., U., R.W.I., F.A., E.S.M.T.E.D., H.A.E.W.K. and F.A.E.S. computed and scrutinized the results. All the authors equally contributed to the writing and proofreading of the paper. All authors reviewed the manuscript.

Competing interests

The authors declare no competing interests.

Additional information

Correspondence and requests for materials should be addressed to W.J.

Reprints and permissions information is available at www.nature.com/reprints.

Publisher's note Springer Nature remains neutral with regard to jurisdictional claims in published maps and institutional affiliations.



Open Access This article is licensed under a Creative Commons Attribution 4.0 International License, which permits use, sharing, adaptation, distribution and reproduction in any medium or format, as long as you give appropriate credit to the original author(s) and the source, provide a link to the Creative Commons licence, and indicate if changes were made. The images or other third party material in this article are included in the article's Creative Commons licence, unless indicated otherwise in a credit line to the material. If material is not included in the article's Creative Commons licence and your intended use is not permitted by statutory regulation or exceeds the permitted use, you will need to obtain permission directly from the copyright holder. To view a copy of this licence, visit <http://creativecommons.org/licenses/by/4.0/>.

© The Author(s) 2022